

Optimization of coupled plasmonic effects for viable phosphorescence of metal-free purely organic phosphor

Cite as: J. Appl. Phys. **122**, 153103 (2017); <https://doi.org/10.1063/1.4997798>

Submitted: 26 July 2017 . Accepted: 29 September 2017 . Published Online: 18 October 2017

Huan Wang, Jaehun Jung, Kyungwha Chung, Ju Won Lim, Youngmin You, Jinsang Kim, and Dong Ha Kim



View Online



Export Citation



CrossMark

ARTICLES YOU MAY BE INTERESTED IN

Voltage tunable plasmon propagation in dual gated bilayer graphene

Journal of Applied Physics **122**, 153101 (2017); <https://doi.org/10.1063/1.5007713>

Polynomial modal method for analysis of the coupling between a gap plasmon waveguide and a square ring resonator

Journal of Applied Physics **122**, 153102 (2017); <https://doi.org/10.1063/1.4999025>

Charge transport in quantum dot organic solar cells with Si quantum dots sandwiched between poly(3-hexylthiophene) (P3HT) absorber and bathocuproine (BCP) transport layers

Journal of Applied Physics **122**, 153104 (2017); <https://doi.org/10.1063/1.4996845>



Optimization of coupled plasmonic effects for viable phosphorescence of metal-free purely organic phosphor

Huan Wang,^{1,a)} Jaehun Jung,^{2,a)} Kyungwha Chung,¹ Ju Won Lim,¹ Youngmin You,³ Jinsang Kim,^{2,b)} and Dong Ha Kim^{1,b)}

¹Department of Chemistry and Nano Science, Ewha Womans University, 52, Ewhayeodae-gil, Seodaemun-gu, Seoul 03760, South Korea

²Department of Macromolecular Science and Engineering, Department of Materials Science and Engineering, Department of Chemistry, and Department of Chemical Engineering, University of Michigan, Ann Arbor, Michigan 48109-2136, USA

³Division of Chemical Engineering and Materials Science, Ewha Womans University, 52, Ewhayeodae-gil, Seodaemun-gu, Seoul 03760, South Korea

(Received 26 July 2017; accepted 29 September 2017; published online 18 October 2017)

Metal-free purely organic phosphorescent molecules are attractive alternatives to organometallic and inorganic counterparts because of their low cost and readily tunable optical properties through a wide chemical design window. However, their weak phosphorescent intensity due to inefficient spin-orbit coupling and, consequently, prevailing non-radiative decay processes limit their practical applicability. Here, we systematically studied phosphorescence emission enhancement of a purely organic phosphor system via plasmon resonance energy transfer. By precisely tuning the distance between purely organic phosphor crystals and plasmonic nanostructures using layer-by-layer assembled polyelectrolyte multilayers as a dielectric spacer, maximum 2.8 and 2.5 times enhancement in photoluminescence intensity was observed when the phosphor crystals were coupled with ~ 55 nm AuNPs and ~ 7 nm AgNPs, respectively, at the distance of 9.6 nm. When the distance is within the range of 3 nm, a dramatic decrease in phosphorescence intensity was observed, while at a larger distance, the plasmonic effect diminished rapidly. The distance-dependent plasmon-induced phosphorescence enhancement mechanism was further investigated by time-resolved photoluminescence measurements. Our results reveal the correlation between the amplification efficiency and plasmonic band, spatial factor, and spectral characteristics of the purely organic phosphor, which may provide an insightful picture to extend the utility of organic phosphors by using surface plasmon-induced emission enhancement scheme. *Published by AIP Publishing.*

<https://doi.org/10.1063/1.4997798>

I. INTRODUCTION

Phosphorescent materials have attracted much attention due to potential applications in display devices, as well as chemical and biological detection.^{1–3} However, most of the efficient phosphors reported to date are essentially inorganics or organometallic complexes.^{4,5} Despite advantageous features of low cost, less toxicity, versatile molecular design, facile functionalization, and good processability, it is difficult to achieve efficient phosphorescence at room temperature and ambient conditions from purely organic molecules. This is because triplet excitons in metal-free organic molecules are mostly consumed through non-radiative processes, such as vibrational dissipation and collisional quenching.⁶ Recently, activation of efficient phosphorescence from purely organic materials has been achieved via controlled crystallization, doping into rigid matrix, and intermolecular interaction in both crystal and amorphous thin films,^{7–17} which were ascribed to the promotion of singlet-to-triplet intersystem crossing through enhanced spin-orbit coupling by the heavy atom effect, restriction of molecular motions

by effective intermolecular interactions, and isolation from oxygen and moisture. Compared to amorphous thin films, crystalline ones show brighter emission and greater stability owing to the highly ordered and dense molecular arrangement in the crystalline form.¹⁸ Furthermore, the rigidity and oxygen-barrier properties of crystals efficiently suppress the non-radiative deactivation pathways of triplet excitons. In our previous study, bright room temperature phosphorescence (RTP) of 2,5-dihexyloxy-4-bromobenzaldehyde (Br6A) and 2,5-dihexyloxy-1,4-dibromobenzene (Br6) mixed crystals was demonstrated at ambient condition in which the directed intermolecular halogen bonding promotes the intersystem-crossing processes by enhancing spin-orbit coupling.

Plasmon-enhanced luminescence (fluorescence or phosphorescence) is a promising optical process that has attracted increasing attention over the past decade, which is induced by the interaction between chromophores and localized surface plasmon resonance (LSPR) from adjacent metallic nanoparticles (NPs) via plasmon resonance energy transfer (PRET).^{19–21} Such phenomenon is affected by a variety of parameters including size and morphology of the metal, as well as the relative distance and spectral overlap between the chromophores and metallic NPs. The plasmon enhancement can be mainly attributed to the increased excitation rate due to

^{a)}H. Wang and J. Jung contributed equally to this work.

^{b)}Authors to whom correspondence should be addressed: jinsang@umich.edu and dhkim@ewha.ac.kr.

a near-field enhancement of excitation and an increased radiation rate of surface plasmon-coupled emission, which can enhance both the photoluminescence (PL) intensity and quantum yield.^{22–24} It is noted that enhanced luminescence reported to date were largely focused on organic fluorophores, inorganic quantum dots, and low-dimensional nanomaterials.^{25–31} Plasmon-induced phosphorescence enhancement (PPE) effect was demonstrated in some organometallics, inorganic phosphors, and purely organic phosphors in close proximity to suitable metallic NPs under cryogenic (e.g., 77 K) and inert conditions.^{32–38} However, PPE with ambient-stability at room-temperature has been rarely reported for purely organic materials.³⁹

Here, we employed Br6A/Br6 mixed crystals as a purely organic phosphor model, size-controlled silver and gold NPs (AgNPs and AuNPs) as a plasmonic nanoantenna, and polyelectrolyte multilayers as a dielectric spacer that can precisely control the distance between the plasmonic nanostructures and the phosphors with a nanoscale precision. Polyelectrolyte multilayers of poly(allylamine hydrochloride) (PAH) and poly(sodium 4-styrenesulfonate) (PSS) deposited on the phosphor crystal layer using the alternating layer-by-layer assembly method were used as a spacer. Size-controlled AgNPs and AuNPs were exploited to control the spectral overlap between the LSPR band of the metal NPs and the excitation/emission wavelengths of the crystals to systematically investigate the spectral overlap effect besides the distance effect, the decisive factor in the enhancement of phosphorescence under ambient conditions. The PPE mechanism was corroborated by dynamic PL study. This work represents comprehensive investigation into PPE phenomenon of purely organic phosphors, which can be recognized as a generally applicable strategy to develop highly efficient hybrid phosphorescence systems.

II. EXPERIMENTAL

A. Synthesis of AuNP (~55 nm) and AgNP (~7 and ~70 nm)

For the synthesis of AuNPs, a solution of 198 ml of deionized water and 2 ml of 1 wt. % Gold(III) chloride hydrate ($\text{HAuCl}_4 \cdot 3\text{H}_2\text{O}$, Aldrich, 99.999%) was heated at 130 °C under vigorous stirring. 1.4 ml of 1 wt. % sodium citrate (Aldrich, 99%) aqueous solution (~10 mg/ml) was then rapidly added, and the solution boiled for additional 30 min under continuous stirring. The AuNPs displayed a hot pink coloration with around 55 nm diameter. For the synthesis of smaller AgNPs (~7 nm), both sodium borohydride (NaBH_4 , Aldrich, 99%) and sodium citrate as the reductants were employed. 3 mg NaBH_4 and 12 mg sodium citrate were dissolved in 148 ml of deionized water. The mixture was heated at 60 °C for 30 min in the dark with vigorous stirring. 2 ml of 23.5 mM silver nitrate (AgNO_3 , Aldrich, >99.8%) solution was then added drop-wise to the mixture and the temperature raised to 90 °C. The pH of solution was adjusted to 10.5 using 0.1 M NaOH while heating was continued for 20 min, until the color of the solution changed to yellow. The diameter size of AgNPs was ~7 nm. For the synthesis of larger AgNPs (~70 nm), sodium citrate as the only reductant was

employed. 7 mg AgNO_3 was dissolved in 150 ml of deionized water and the mixture was heated to boiling point. Then, 3 ml of 1 wt. % sodium citrate aqueous solution was added to the boiling solution, and boiling was maintained for 1 h, yielding ~70 nm diameter AgNPs. Figures S1(a)–S1(c) (supplementary material) show higher resolution scanning electron microscopy (SEM) images of the synthesized metallic NPs, and the average diameter and size distribution of the NPs are shown in (d).

B. Fabrication of plasmon-mediated Br6A/Br6 crystals

Br6A and Br6 were synthesized referring to the previous report (Ref. 8). 1 wt. % mixture of Br6A to Br6 in hexane solution with the concentration of 5 mg/ml was spin-coated (2000 rpm) on the clean glass substrate for the pristine crystal preparation. PAH with average Mw of ~17 500 g/mol and PSS with average Mw of ~70 000 g/mol were purchased in Sigma-Aldrich, which were dissolved in 3.3 mM sodium chloride (NaCl) solution controlled to the concentration of 0.5 mg/ml before use. Polyelectrolyte multilayers of positively charged PAH and negatively charged PSS were assembled alternatively for 5 min using the immersion-based layer-by-layer self-assembly procedure. After each step (PAH or PSS), the sample was rinsed with ultrapure deionized water. The process was repeated to obtain desired numbers of polyelectrolyte multilayers. A PAH layer was used at the outermost surface to promote the adhesion of the negatively charged citrate-passivated AuNPs or AgNPs.

C. Characterization techniques

The wide-angle XRD was detected with a Rigaku X-ray diffractometer (D/Max-rA, using Cu-K α radiation of wavelength 1.542 Å). Absorbance was measured using an Agilent Cary 5000 UV-Vis-NIR spectrometer. Surface morphologies were obtained using AFM in tapping mode (Digital Instrument Dimension 3100 scanning force microscope) and scanning electron microscopy (SEM; JEOL JSM6700-F). Surface plasmon resonance (SPR) spectroscopy measurements (Resonant Technologies GmbH/RT2005 SPR spectrometer) were carried out using *p*-polarized laser light (He–Ne, 632.8 nm, 10 mW) illuminating the Au film through the LaSFN9 prism. Calculation of PSS/PAH thickness was carried out using Winspall software (RES-TEC, Germany) with the complex refractive index and dielectric constant values of 1.45 and 2.0125, respectively. It was assumed that PAH and PSS have the same values for optical constants. Finite-difference time-domain (FDTD) simulation was carried out using Lumerical Solution software. The mesh size was set at 0.5 nm for the elaborate design. The plane wave source was used as incident light. *z* and *x* were considered to be the light incident direction and the polarization direction, respectively. PL spectra were obtained using a Photon Technologies International (PTI), QuantaMaster 400 scanning spectrofluorimeter at 298 K. Phosphorescent lifetime data were collected using a PTI LaserStrobe and the calculations were carried out on the FeliX32 software partnered with the PTI equipment.

III. RESULTS AND DISCUSSION

Figure 1(a) shows the molecular structures of Br6A and Br6. In the earlier study, Br6A with halogenated aromatic aldehyde can only produce fluorescent emission in the disordered state (e.g., in solution) where there is no halogen bond, because the vibrational loss of triplets is strong, making triplet emission inefficient or inactive.⁸ When the halogen-bond formation between aldehyde and bromine in the crystalline state brings aromatic carbonyls and the heavy atom effect together in an unprecedented synergy, triplets are generated very efficiently, which suppresses fluorescence, and phosphorescence is activated by enhanced spin-orbit coupling to the ground state and reduced vibrational freedom of the aldehyde.⁸ It has been also demonstrated that Br6A molecules doped into the host Br6 crystal matrix can emit much more efficient phosphorescence by preventing excimer-induced self-quenching. In this work, 1 wt. % Br6A-doped Br6 crystal has been prepared to combine with different plasmonic nanometals as the PPE systems to investigate.⁹ The excitation and phosphorescence spectra of Br6A/Br6 mixed crystals and the fluorescence spectrum of Br6A single molecule in solution are shown in Fig. 1(b), corresponding to the wavelengths of 385, 520, and 420 nm, respectively. Figure 1(c) depicts the schematic models of LSPR field enhancement effects on the luminescence enhancement in term of the spectral proximity. For comprehensively understanding the plasmonic effects of metallic NPs on the phosphorescence enhancement, size-controlled AgNPs (~ 7 and ~ 70 nm) and

AuNPs (~ 55 nm) have been employed, in which their LSPR bands have a substantial overlap with the excitation, fluorescence, or phosphorescence wavelengths of the chromophore, respectively.

Figure 2(a) schematically illustrates the fabrication strategy of the plasmon-mediated Br6A/Br6 mixed crystals with thickness-controlled polyelectrolyte multilayers as the spacer. The initially formed crystals spin-coated on the glass substrate were around $\sim 3 \mu\text{m}$ in size and ~ 600 nm in thickness (Step I). For increasing the crystal size and spread the crystals on the substrate more evenly so as to achieve more consistent and sensitive plasmonic effect, the pristine Br6A/Br6 crystals were further heat treated at 70°C , which gave a thin Br6A/Br6 crystal layer having a larger than $20 \mu\text{m}$ size and ~ 90 nm thickness (Step II) as shown in the optical microscopy and magnified AFM images [Fig. 2(a)]. Then, polyelectrolyte multilayers of positively charged PAH and negatively charged PSS were alternately deposited on the crystals. The thickness of the dielectric spacer can be precisely controlled on the nanometer scale (Step III). Eventually, metallic NPs were dip-coated on top of the polyelectrolyte layers (Step IV). By using this well-defined organic phosphors/dielectric spacer/metallic nanoparticle tri-layer platform, the effects of the distance between phosphors and plasmonic nanometals and the spectral overlap on PPE were systematically investigated. The dark field images of the pristine crystal and ~ 55 nm AuNPs-decorated crystals with a spacer thickness of ~ 1.6 and ~ 9.6 nm, respectively, clearly show the distance-dependent emission amplification (Step V).

The thickness of alternating polyelectrolyte multilayers of PAH and PSS was analyzed by means of surface plasmon resonance (SPR) spectroscopy. SPR is a unique optical phenomenon observed at the metal-dielectric interface in nano-scale dimension, and the resonance band position depends on various parameters including the optical property of the prism, type of metal, thickness, and refractive index of the dielectric medium in contact with the metal, wavelength of the light source, etc. The thickness of the polyelectrolyte multilayers was evaluated by means of the same strategy reported in the literature.^{40,41} Figure 2(b) shows the series of scan mode SPR angular curves of the layer-by-layer electrostatic self-assembled polyelectrolyte multilayers. The SPR angle shifted progressively to a higher incident angle as the number of polyelectrolyte layers increased from a single layer to 16 multilayers [alternating PSS (–) and PAH (+)]. Broadening of the curves and increase in the reflectivity were observed as the number of polyelectrolyte layers increased because the increased surface roughness induces more light scattering. For quantifying the thickness from the SPR data, we conducted a simulation study by using Winspall software and obtained the linear correlation between the number of polyelectrolyte layers and the thickness of the film as shown in Fig. 2(c). It was estimated that the 6 multilayers was ~ 9.6 nm thick, which means that the average thickness of each layer is about 1.6 nm. For double confirming the film thickness, we also used a cross-sectional AFM image along the step formed by an intentional scratch on the polyelectrolyte film. The AFM height profile shows that the thickness of 8-multilayer polyelectrolytes is

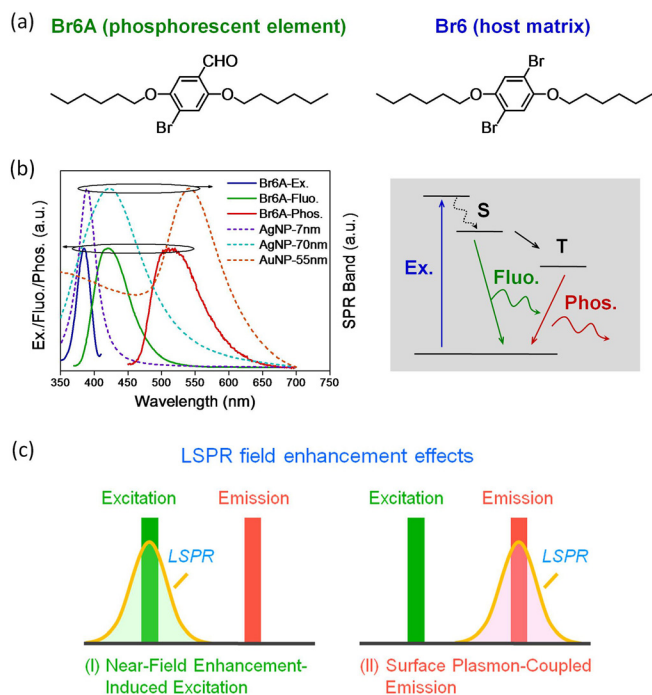


FIG. 1. (a) Molecular structures of Br6A and Br6. (b) LSPR bands of AgNP with ~ 7 and ~ 70 nm diameter, and AuNP with ~ 55 nm diameter; excitation, fluorescence, and phosphorescence wavelengths of the chromophore.⁸ (c) Schematic models representing LSPR field enhancement effects on the luminescence enhancement. Near-field enhancement-induced excitation (I) and surface plasmon-coupled emission (II) can be realized by matching the LSPR band with the excitation and emission wavelength of the organic crystals, respectively.

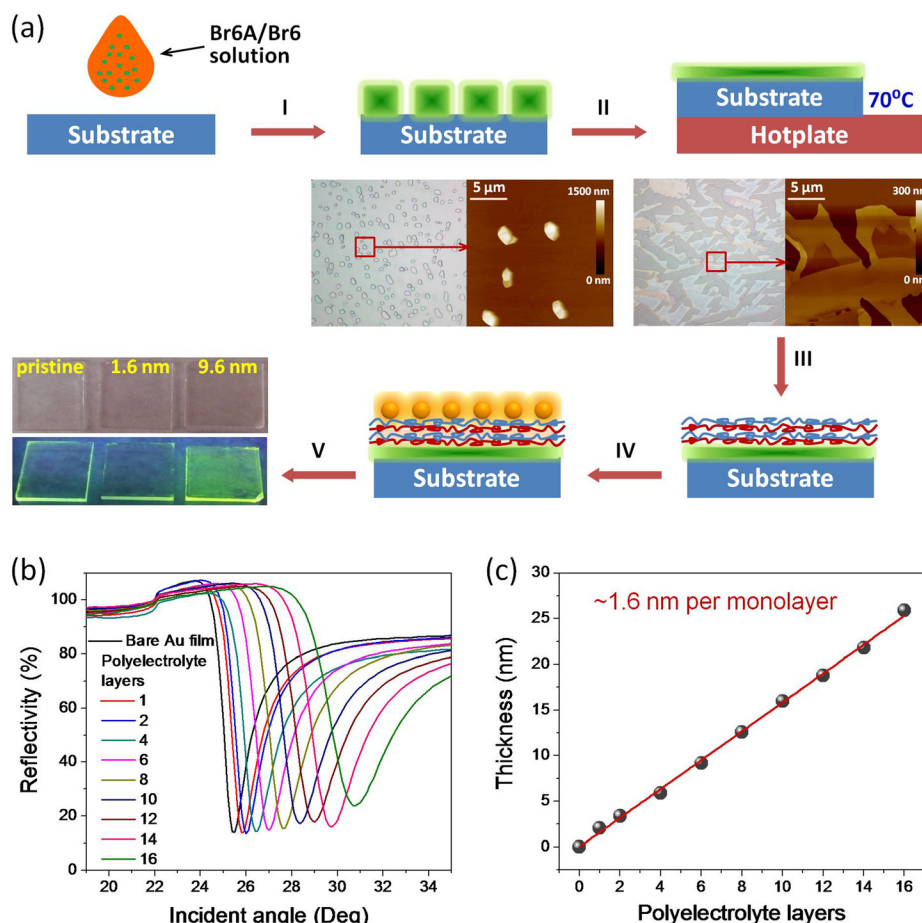


FIG. 2. (a) Schematic illustration of the entire procedure to fabricate plasmon-mediated Br6A/Br6 crystal samples: I. Thicker and smaller crystals prepared by spin-coating (the crystal size is $\sim 3 \mu\text{m}$ with $\sim 600 \text{ nm}$ thickness); II. Thinner and larger crystal formed by heating (the crystal size is larger than $20 \mu\text{m}$ with $\sim 90 \text{ nm}$ thickness); III. Alternate layer-by-layer self-assembly of polyelectrolyte multilayers; IV. Deposition of metallic NPs by electrostatic interaction; V. Photographs of pristine crystal and $\sim 55 \text{ nm}$ AuNPs-decorated crystals with two different thickness of polyelectrolyte layers (~ 1.6 and $\sim 9.6 \text{ nm}$) under normal room light and 365 nm ultraviolet light, respectively. (b) Static scan-mode SPR spectroscopy profile monitoring the stepwise deposition of PSS and PAH polyelectrolyte multilayers on a bare Au film coated on the glass substrate. (c) The calculated film thickness as a function of the number of polyelectrolyte layers. The average thickness of each layer was estimated to be $\sim 1.6 \text{ nm}$.

$\sim 12.2 \text{ nm}$ (Fig. S2, [supplementary material](#)), which is in good agreement with the calculated $\sim 12.8 \text{ nm}$ from the SPR method.

The amount of metallic NPs deposited on the surface of the polyelectrolyte multilayer was tuned by controlling the dipping time of the substrate in the prepared plasmonic nanometal suspensions. Due to the negative surface charges of the citrate-passivated AuNPs and AgNPs, these NPs adhere to the PAH layer at the surface of the polyelectrolyte multilayer. Representative SEM images showing the distribution of $\sim 55 \text{ nm}$ AuNPs are displayed in Figs. S3(a)–S3(e) ([supplementary material](#)). The surface density of AuNPs deposited for the dipping time of 15, 45, 60, 90, and 120 min is 13, 28, 45, 61, and $70/\mu\text{m}^2$, respectively. The absorbance profile of the adsorbed AuNPs is shown in Fig. S3(f), [supplementary material](#). One can clearly see that the intensity of the characteristic LSPR band at $\sim 540 \text{ nm}$ increases proportionally with the AuNPs density. The distribution and corresponding absorbance of the ~ 7 and $\sim 70 \text{ nm}$ AgNPs are also shown in Figs. S4 and S5, [supplementary material](#).

The distance-dependent PPE phenomenon was first analyzed on the premise of optimal density for each metallic NPs. As shown in Fig. 1(b), ~ 7 and $\sim 70 \text{ nm}$ AgNPs and $\sim 55 \text{ nm}$ AuNPs as plasmonic nanoantenna have substantial overlap of their LSPR bands with the excitation, fluorescence, or phosphorescence wavelengths of the organic phosphors, respectively. In Fig. 3(a), PL spectra obtained from Br6A/Br6 crystals with AuNPs (or AgNPs) separated by ~ 1.6 , 3.2 , 6.4 , 9.6 , 12.8 , 16.0 , and 19.2 nm spacing

(corresponding to 1, 2, 4, 6, 8, 10, and 12 polyelectrolyte multilayers), respectively, are displayed. The maximum PL intensity for the plasmon-mediated Br6A/Br6 crystals was observed from the sample with a $\sim 9.6 \text{ nm}$ thick spacer followed by a gradual decrease in the PL intensity with increase in the polyelectrolyte thickness. When the polyelectrolyte thickness was close to $\sim 20 \text{ nm}$, the PL intensity became comparable with that of the pristine Br6A/Br6 crystals on a bare glass substrate as a reference [Fig. 3(b)], indicating that the chromophores placed far from the metallic surface are not significantly influenced by the enhanced electromagnetic field of plasmonic nanometals. Figure 3(c) shows the photographs of the plasmon-mediated Br6A/Br6 crystals with different polyelectrolyte thickness under 365 nm ultraviolet light. The maximum enhancement for the $\sim 55 \text{ nm}$ AuNPs, ~ 7 and $\sim 70 \text{ nm}$ AgNPs were up to 2.8, 2.5 and 1.8 times, respectively (Table S1, [supplementary material](#)). It is noted that the fluorescence emission of Br6A/Br6 crystals at 420 nm was barely detectable excluding the influence of surface plasmon-coupled emission for the case of $\sim 70 \text{ nm}$ AgNPs. Thus, it is assumed that the phosphorescence enhancement might stem from partial overlap of the LSPR band with the excitation wavelength of Br6A/Br6 crystals. It is also noteworthy that quenching of PL intensity was induced at a very short distance ($< 3 \text{ nm}$) between the phosphors and plasmonic nanometals due to the existence of trap states and direct energy transfer (DET) at the metallic surfaces.^{26,42} Therefore, the competition between LSPR field enhancement and metal-induced quenching is the crucial

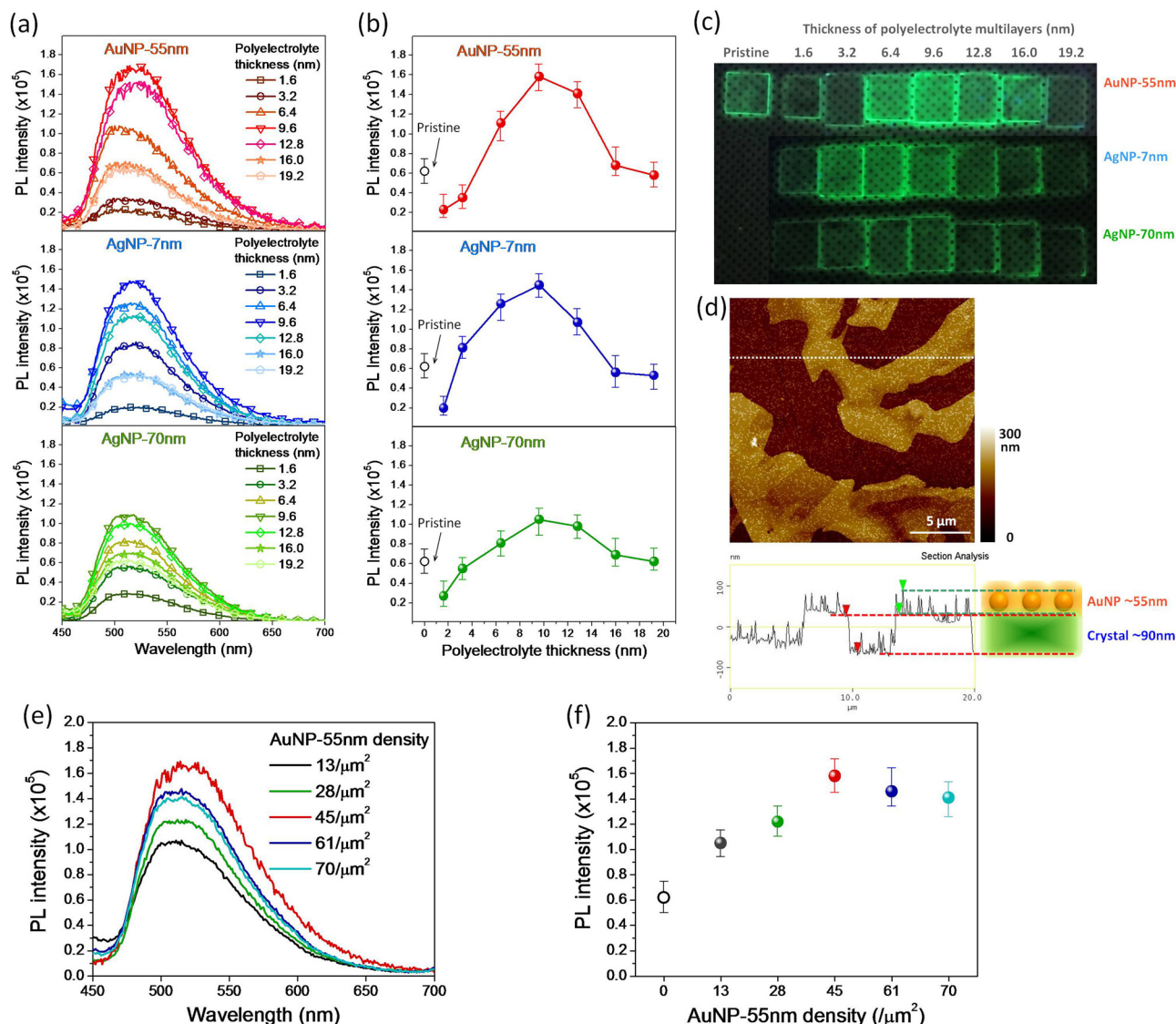


FIG. 3. (a) PL spectra of different plasmon-mediated phosphorescent Br6A/Br6 crystals with different thickness of polyelectrolyte multilayer spacers (from 1.6 to 19.2 nm). (b) Statistical comparison (over 10 samples for each case) of PL intensity described in (a). (c) Photographs of pristine crystal, and the ones decorated with ~55 nm AuNPs, ~7 nm AgNPs, and ~70 nm AgNPs with different thicknesses of polyelectrolyte multilayers under 365 nm ultraviolet light. (d) AFM morphology of ~55 nm AuNPs-decorated crystal film. From the section analysis, the height of AuNPs nanostructure constructed on the crystals was measured to be around 55 nm and the crystal thickness is around 90 nm. (e) PL spectra of plasmon-mediated phosphorescent Br6A/Br6 crystals with different density of ~55 nm AuNPs by controlling the dipping time. (f) Statistical comparison (over 10 samples for each case) of PL intensity described in (e). For all samples, the polyelectrolyte thickness was adjusted to ~9.6 nm (6 multilayers).

factor in the distance-dependent PPE phenomenon. A detailed PPE mechanism is discussed in more detail later. Figure 3(d) shows an AFM image of the Br6A/Br6 crystals with ~55 nm AuNPs. AuNPs are distributed uniformly on the entire surface of the positively charged PAH layer on top of the crystals. From the section analysis, the average thickness of AuNPs nanostructure constructed on the crystals was around 55 nm and that of the crystals was around 90 nm. Uniform decoration of ~7 and ~70 nm AgNPs onto the crystals was also confirmed by the AFM images as shown in Fig. S6, [supplementary material](#).

For investigating how the amount of plasmonic NPs affects the phosphorescence emission intensity of Br6A/Br6 crystals, the samples, having a fixed thickness of ~9.6 nm polyelectrolyte multilayers but different surface density of

~55 nm AuNPs, were fabricated. Their PL spectra were collected under a 380 nm excitation wavelength as shown in Fig. 3(e). Compared to the pristine sample without having AuNPs, all plasmon-mediated samples manifest phosphorescence enhancement [Fig. 3(f)]. The enhancement of PL intensity linearly increased with the surface density of AuNPs initially but slightly decreased after a maximum point. Although we do not fully understand why the phosphorescence enhancement is not fully linear with through the entire range of AuNP amount, the observed saturating or less efficient enhancement at the larger AuNP density may be caused by a slight degradation of the sample immersed into the nano-suspension for a longer time or increased nonradiative energy transfer from the phosphor crystal to AuNPs competing with the LSPR field enhancement effects.^{21,43,44}

It was found that $\sim 45/\mu\text{m}^2$ density of AuNPs was optimal for maximum PPE and the optimized values for the ~ 7 and ~ 70 nm AgNPs were 1100 and $39/\mu\text{m}^2$, respectively.

Figures 4(a)–4(c) show the PL decays of phosphorescent Br6A/Br6 crystals, in combination with ~ 55 nm AuNPs, ~ 7 nm AgNPs, or ~ 70 nm AgNPs separated by the differing thickness of polyelectrolyte multilayer spacer, respectively. The lifetime obtained by fitting the decay curves is summarized in Fig. 4(d). The pristine crystal showed the longest lifetime up to ~ 8.08 (± 0.41) ms, compared to those of the plasmon-mediated crystals. For the samples decorated with ~ 55 nm AuNPs, ~ 7 nm AgNPs, or ~ 70 nm AgNPs, the

lifetime decreased to ~ 7.49 (± 0.39), 7.65 (± 0.44), and 7.24 (± 0.45) ms, respectively, when the distance between the crystals and the plasmonic nanostructures was ~ 1.6 nm. It is verified that excited electrons are quenched by the metallic NPs judging from the sharp decrease in their PL intensity at this close spacing. When the polyelectrolyte layer thickness was ~ 9.6 nm, the lifetime of the same samples was measured to be ~ 7.36 (± 0.47), 7.99 (± 0.38), and 7.37 (± 0.31) ms, respectively. The shorter lifetime combined with the enhanced PL intensity than those of the pristine crystal can be attributed to the LSPR field enhancement effects amplifying excitation and accelerating radiation rate.^{31,45} At

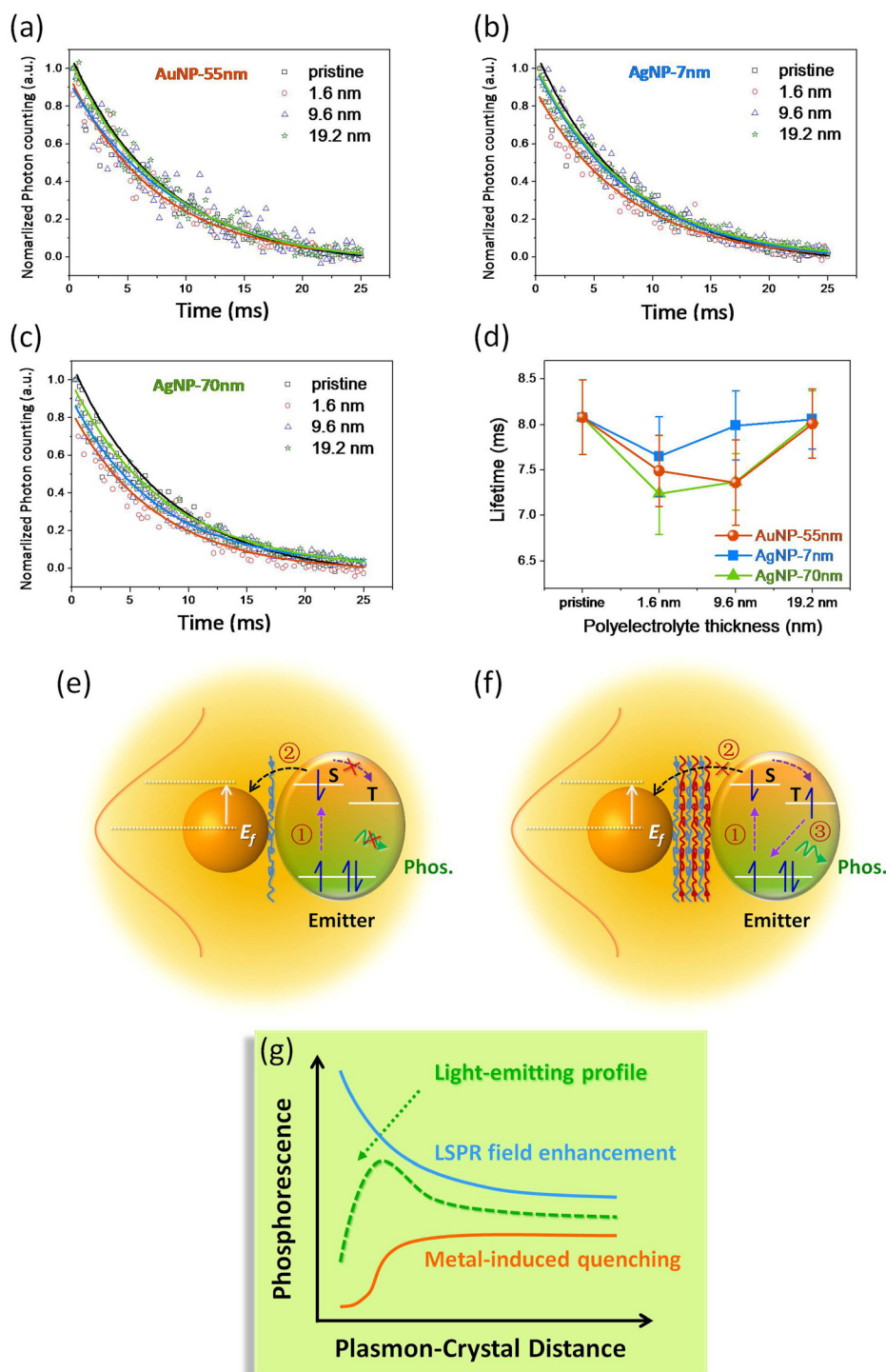


FIG. 4. PL decay curves of different plasmon-mediated phosphorescent Br6A/Br6 crystals (pristine crystal as the reference) monitoring the 520 nm emission under 380 nm excitation for various thicknesses of polyelectrolyte multilayer spacers: (a) ~ 55 nm AuNPs; (b) ~ 7 nm AgNPs; (c) ~ 70 nm AgNPs. (d) Fitted lifetime comparison of above samples. The schematic mechanism of quenched and enhanced phosphorescence: (e) Metal-induced quenching is dominant when the distance between plasmonic nanometal and emitter is short, causing a quenching of PL; (f) LSPR field enhancement is dominant when the distance between plasmonic nanometal and emitter is optimized, leading to an enhancement of PL. (g) Schematic diagram of the emission distribution varying with the distance between plasmonic nanometals and phosphor crystals by the combined influence of metal-induced quenching and LSPR field enhancement. Processes ①, ②, and ③ represent the excitation, metal-induced quenching, and radiation, respectively.

the polyelectrolyte spacer thickness of ~ 19.2 nm, the phosphorescence lifetime was ~ 8.01 (± 0.38), 8.06 (± 0.33), and 8.05 (± 0.32) ms close to the lifetime of the pristine crystal, reflecting the diminished plasmonic effect. The PL lifetime of the above samples are summarized in Table I.

When phosphor crystals are very close to plasmonic nanometals (< 3 nm), the DET from the crystal to the NP leads to drastic PL quenching, which is in agreement with previous works observed for other molecular systems.^{26,42,46} Besides the DET, electrons from photoexcited electron-hole pairs in the crystal can tunnel to and be captured in the NP followed by nonradiative recombination with remaining holes at the semiconductor-metal interface due to the existence of trap states at the metallic surfaces. Hence, both factors can induce metal-induced quenching occurring at the short distance between plasmonic nanometals and phosphor crystals [Fig. 4(e)]. With an increasing thickness of polyelectrolyte layers, the DET becomes less efficient and the probability of photoelectron tunneling into the metallic nanoparticle is also drastically diminished. With the suppression of metal-induced quenching, LSPR field enhancement effects on PPE becomes dominant [Fig. 4(f)]. In the case of 55 nm AuNPs, surface plasmon-coupled emission originated from the spectral overlap between the phosphorescence emission and the AuNP LSPR band accelerates the radiation rate and results in an enhancement of PL intensity. When it comes to the AgNPs, near-field enhancement-induced excitation from the overlap of the AgNP LSPR band with the excitation wavelength of Br6A/Br6 crystals accelerates the excitation rate, and thereby increases the rate of singlet-to-triplet intersystem crossing, eventually leading to an enhancement of PL intensity. In Fig. 4(g), the two competing processes, the metal-induced quenching and LSPR field enhancement effects, dictating the light-emitting profile are schematically described. The optimum distance between plasmonic nanometals and phosphor crystals was found to be ~ 9.6 nm for attaining the maximum phosphorescence enhancement. If the crystal is too close or too far from the NP, PPE is either diminished because of dominant metal-induced quenching or a weak electromagnetic field.

In the case of localized surface plasmons, the coherent oscillations are confined to a small region, which gives the enhanced near-field amplitude at the resonance wavelength. This electromagnetic field is highly localized around the plasmonic nanometal and decays rapidly away from the NP/dielectric interface into the dielectric background. Finite-

difference time-domain (FDTD) simulations were employed to estimate the LSPR field enhancement at the surface of plasmonic nanometals used in this study. As shown in Fig. S7 (supplementary material), it is clearly observed that the electric field intensity around AgNP is higher than that of AuNP for 380 nm excitation, indicating the more effective near-field enhancement-induced excitation from the overlap of the AgNP LSPR band with the excitation maximum wavelength (λ_m) of Br6A/Br6 crystal. Upon excitation at 520 nm, the electric field intensity around AuNP, in turn, becomes much higher, which favors surface plasmon-coupled emission due to the spectral overlap between the phosphorescence emission and the AuNP LSPR band. FDTD simulations verified that the stronger LSPR field enhancement was generated surrounding AgNP and AuNP, contributing to the enhancement in PL intensity of the Br6A/Br6 crystals.

IV. CONCLUSIONS

In summary, distance-dependent enhancement of phosphorescence from purely organic phosphor Br6A/Br6 crystals combined with plasmonic nanometals was investigated using layer-by-layer assembled polyelectrolyte multilayers as a dielectric spacer. Maximum 2.8 and 2.5 times enhancement in PL intensity was observed when Br6A/Br6 crystals were spaced about 9.6 nm from ~ 55 nm AuNPs and ~ 7 nm AgNPs, respectively. This is attributed to the substantial overlap of the phosphorescence or excitation wavelength of Br6A/Br6 crystals with the LSPR bands of AuNPs and AgNPs, which can accelerate the radiation and excitation rate as evidenced by time-resolved PL measurements. The significant decrease in PL intensity was also observed at a very close spacing between Br6A/Br6 crystals and plasmonic nanometals. Hence, distance-dependent plasmon-induced phosphorescence enhancement arises from the competitive interplay between LSPR field enhancement and metal-induced quenching. This study is the first thorough investigation on phosphorescence enhancement mechanism of purely organic phosphors by the plasmonic effect under ambient conditions. Our findings also verify that proper spectral overlap between the excitation and phosphorescence emission of the purely organic phosphors and the LSPR bands of plasmonic nanometals can effectively enhance the phosphorescence emission intensity and efficiency. The presented PPE strategy can be generally applicable to other purely organic phosphors. For example, considering that the longitudinal band of Au nanorods (AuNRs) can be tuned by the aspect ratio, locating AuNRs' plasmonic band in the range of red to near-infrared AuNRs²² would be a feasible plasmonic nano-antenna for effectively amplifying purely organic red phosphors⁸ for future application of PPE strategy for full color organic light-emitting diodes (OLEDs).

SUPPLEMENTARY MATERIAL

See supplementary material for microscopic images of metal nanoparticles, surface of layer-by-layer self-assembled multilayers, FDTD simulation result for the electric field

TABLE I. Summary of PL lifetime of different plasmon-mediated Br6A/Br6 crystals with different thicknesses of polyelectrolyte layers.

Thickness of polyelectrolyte layers (nm)	~ 55 nm AuNP		~ 7 nm AgNP		~ 70 nm AgNP	
	Lifetime (ms)	Error (ms)	Lifetime (ms)	Error (ms)	Lifetime (ms)	Error (ms)
Pristine (Ref.)	8.08	0.41	8.08	0.41	8.08	0.41
1.6	7.49	0.39	7.65	0.44	7.24	0.45
9.6	7.36	0.47	7.99	0.38	7.37	0.31
19.2	8.01	0.38	8.06	0.33	8.05	0.32

distribution and a summary table of PL intensity of plasmon-mediated organic crystals are provided.

AFM images of polyelectrolyte multilayers and AgNPs-decorated crystals (Figs. S2 and S6); SEM images of the dispersed metallic NPs, and the NP diameters and corresponding absorbance profiles (Figs. S1 and S3–S5); electric field distributions around different NPs from FDTD simulations (Fig. S7). Summary of the maximum enhancement of the PL intensity for each plasmon-mediated sample (Table S1).

ACKNOWLEDGMENTS

This work was supported by the National Research Foundation of Korea Grant funded by the Korean Government (2017R1A2A1A05022387). We also acknowledge the financial support from NSF (DMREF DMR 143965) and Samsung GRO Grant.

- ¹M. A. Baldo, D. F. O'Brien, Y. You, A. Shoustikov, S. Sibley, M. E. Thompson, and S. R. Forrest, *Nature* **395**, 151 (1998).
- ²Y. You, Y. Han, Y.-M. Lee, S. Y. Park, W. Nam, and S. J. Lippard, *J. Am. Chem. Soc.* **133**, 11488 (2011).
- ³Q. Zhao, C. Huang, and F. Li, *Chem. Soc. Rev.* **40**, 2508 (2011).
- ⁴B. Wang, H. Lin, J. Xu, H. Chen, Z. Lin, F. Huang, and Y. Wang, *Inorg. Chem.* **54**, 11299 (2015).
- ⁵V. W.-W. Yam, V. K.-M. Au, and S. Y.-L. Leung, *Chem. Rev.* **115**, 7589 (2015).
- ⁶A. Köhler, J. S. Wilson, and R. H. Friend, *Adv. Mater.* **14**, 701 (2002).
- ⁷W. Z. Yuan, X. Y. Shen, H. Zhao, J. W. Y. Lam, L. Tang, P. Lu, C. Wang, Y. Liu, Z. Wang, Q. Zheng, J. Z. Sun, Y. Ma, and B. Z. Tang, *J. Phys. Chem. C* **114**, 6090 (2010).
- ⁸O. Bolton, K. Lee, H.-J. Kim, K. Y. Lin, and J. Kim, *Nat. Chem.* **3**, 205 (2011).
- ⁹O. Bolton, D. Lee, J. Jung, and J. Kim, *Chem. Mater.* **26**, 6644 (2014).
- ¹⁰H. Y. Gao, X. R. Zhao, H. Wang, X. Pang, and W. J. Jin, *Cryst. Growth Des.* **12**, 4377 (2012).
- ¹¹Y. Gong, L. Zhao, Q. Peng, D. Fan, W. Z. Yuan, Y. Zhang, and B. Z. Tang, *Chem. Sci.* **6**, 4438 (2015).
- ¹²H. Shi, Z. An, P.-Z. Li, J. Yin, G. Xing, T. He, H. Chen, J. Wang, H. Sun, W. Huang, and Y. Zhao, *Cryst. Growth Des.* **16**, 808 (2016).
- ¹³S. Hirata, K. Totani, J. Zhang, T. Yamashita, H. Kaji, S. R. Marder, T. Watanabe, and C. Adachi, *Adv. Funct. Mater.* **23**, 3386 (2013).
- ¹⁴D. Lee, O. Bolton, B. C. Kim, J. H. Youk, S. Takayama, and J. Kim, *J. Am. Chem. Soc.* **135**, 6325 (2013).
- ¹⁵M. S. Kwon, D. Lee, S. Seo, J. Jung, and J. Kim, *Angew. Chem., Int. Ed.* **126**, 11359 (2014).
- ¹⁶M. S. Kwon, Y. Yu, C. Coburn, A. W. Phillips, K. Chung, A. Shanker, J. Jung, G. Kim, K. Pipe, S. R. Forrest, J. H. Youk, J. Gierschner, and J. Kim, *Nat. Commun.* **6**, 8947 (2015).
- ¹⁷Z. An, C. Zheng, Y. Tao, R. Chen, H. Shi, T. Chen, Z. Wang, H. Li, R. Deng, X. Liu, and W. Huang, *Nat. Mater.* **14**, 685 (2015).
- ¹⁸H. Wang, Y. Zhao, Z. Xie, H. Shang, H. Wang, F. Li, and Y. Ma, *CrystEngComm* **17**, 2168 (2015).
- ¹⁹P. P. Pompa, L. Martiradonna, A. Della Torre, F. Della Sala, L. Manna, M. De Vittorio, F. Calabi, R. Cingolani, and R. Rinaldi, *Nat. Nanotechnol.* **1**, 126 (2006).
- ²⁰S. Khatua, P. M. R. Paulo, H. Yuan, A. Gupta, P. Zijlstra, and M. Orrit, *ACS Nano* **8**, 4440 (2014).
- ²¹S. T. Kochuveedu and D. H. Kim, *Nanoscale* **6**, 4966 (2014).
- ²²N. Gandra, C. Portz, L. Tian, R. Tang, B. Xu, S. Achilefu, and S. Singamaneni, *Angew. Chem., Int. Ed.* **53**, 866 (2014).
- ²³S.-H. Cao, W.-P. Cai, Q. Liu, and Y.-Q. Li, *Annu. Rev. Anal. Chem.* **5**, 317 (2012).
- ²⁴M. Saboktakin, X. Ye, S. J. Oh, S.-H. Hong, A. T. Fafarman, U. K. Chettiar, N. Engheta, C. B. Murray, and C. R. Kagan, *ACS Nano* **6**, 8758 (2012).
- ²⁵A. Camposeo, L. Persano, R. Manco, Y. Wang, P. Del Carro, C. Zhang, Z.-Y. Li, D. Pisignano, and Y. Xia, *ACS Nano* **9**, 10047 (2015).
- ²⁶O. Kulakovich, N. Strekal, A. Yaroshevich, S. Maskevich, S. Gaponenko, I. Nabiev, U. Woggon, and M. Artemyev, *Nano Lett.* **2**, 1449 (2002).
- ²⁷Z. Q. Li, S. Chen, J. J. Li, Q. Q. Liu, Z. Sun, Z. B. Wang, and S. M. Huang, *J. Appl. Phys.* **111**, 014310 (2012).
- ²⁸S. Butun, S. Tongay, and K. Aydin, *Nano Lett.* **15**, 2700 (2015).
- ²⁹J. Miao, W. Hu, Y. Jing, W. Luo, L. Liao, A. Pan, S. Wu, J. Cheng, X. Chen, and W. Lu, *Small* **11**, 2392 (2015).
- ³⁰W. Liu, B. Lee, C. H. Naylor, H.-S. Ee, J. Park, A. T. C. Johnson, and R. Agarwal, *Nano Lett.* **16**, 1262 (2016).
- ³¹S. T. Kochuveedu, T. Son, Y. Lee, M. Lee, D. Kim, and D. H. Kim, *Sci. Rep.* **4**, 4735 (2014).
- ³²M. J. R. Previte, K. Aslan, Y. Zhang, and C. D. Geddes, *J. Phys. Chem. C* **111**, 6051 (2007).
- ³³D. Chaudhuri, D. Li, E. Sigmund, H. Wettach, S. Höger, and J. M. Lupton, *Chem. Commun.* **48**, 6675 (2012).
- ³⁴M. Kim, S. M. Lee, and K. C. Choi, *App. Phys. Lett.* **105**, 141119 (2014).
- ³⁵Y. Zhang, K. Aslan, S. N. Malyn, and C. D. Geddes, *Chem. Phys. Lett.* **427**, 432 (2006).
- ³⁶Y. Zhang, K. Aslan, M. J. R. Previte, S. N. Malyn, and C. D. Geddes, *J. Phys. Chem. B* **110**, 25108 (2006).
- ³⁷R. Toftegaard, J. Arnbjerg, K. Daasbjerg, P. R. Ogilby, A. Dmitriev, D. S. Sutherland, and L. Poulsen, *Angew. Chem., Int. Ed.* **47**, 6025 (2008).
- ³⁸O. Planas, N. Macia, M. Agut, S. Nonell, and B. Heyne, *J. Am. Chem. Soc.* **138**, 2762 (2016).
- ³⁹C. Seo, J. Lee, M. S. Kim, Y. Lee, J. Jung, H.-W. Shin, T. K. Ahn, G. Sun, J. Kim, and J. Kim, *Chem. Phys. Lett.* **676**, 134 (2017).
- ⁴⁰K. Chung, A. Rani, J.-E. Lee, J. E. Kim, Y. Kim, H. Yang, S. O. Kim, D. Kim, and D. H. Kim, *ACS Appl. Mater. Interfaces* **7**, 144 (2015).
- ⁴¹A. Rani, K. Chung, J. Kwon, S. J. Kim, Y. H. Jang, Y. J. Jang, L. N. Quan, M. Yoon, J. H. Park, and D. H. Kim, *ACS Appl. Mater. Interfaces* **8**, 11488 (2016).
- ⁴²P. Reineck, D. Gómez, S. H. Ng, M. Karg, T. Bell, P. Mulvaney, and U. Bach, *ACS Nano* **7**, 6636 (2013).
- ⁴³C. Rohner, I. Tavernaro, L. Chen, P. J. Klar, and S. Schlecht, *Phys. Chem. Chem. Phys.* **17**, 5932 (2015).
- ⁴⁴N. A. Harun, M. J. Benning, B. R. Horrocks, and D. A. Fulton, *Nanoscale* **5**, 3817 (2013).
- ⁴⁵X. Wu, L. Liu, W. C. H. Choy, T. Yu, P. Cai, Y. Gu, Z. Xie, Y. Zhang, L. Du, Y. Mo, S. Xu, and Y. Ma, *ACS Appl. Mater. Interfaces* **6**, 11001 (2014).
- ⁴⁶T. Gryczynski, J. Malicka, Y. Shen, Z. Gryczynski, and J. R. Lakowicz, *J. Phys. Chem. B* **106**, 2191 (2002).